

# Photon echoes in strongly scattering media: a diagrammatic approach

R. Pierrat,<sup>1</sup> R. Carminati,<sup>1</sup> and J.-L. Le Gouët<sup>2</sup>

<sup>1</sup>*ESPCI Paris, Université PSL, CNRS, Institut Langevin, 1 rue Jussieu, F-75005, Paris, France\**

<sup>2</sup>*Laboratoire Aimé Cotton, CNRS, Université Paris-Sud,  
ENS Cachan, Université Paris-Saclay, F-91405, Orsay Cedex, France*

We study photon echo generation in disordered media with the help of multiple scattering theory based on diagrammatic approach and numerical simulations. We show that a strong correlation exists between the driving fields at the origin of the echo and the echo beam. Opening the way to a better understanding of non-linear wave propagation in complex materials, this work supports recent experimental results with applications to the measurement of the optical dipole lifetime  $T_2$  in powders.

## I. INTRODUCTION

Wave scattering in disordered media has attracted considerable attention for decades. First undertaken within the general scope of the multiple scattering theory, in close connection with quantum mechanics [1–3], investigations later focused on classical waves and optical processes, revealing features such as the backscattering peak [4, 5] or random lasing [6, and references therein]. Wave propagation in complex media can also be combined with nonlinear optics [7, 8]. In the specific framework of four-wave mixing (FWM), it has been recognized quite early that coherent anti-Stokes Raman scattering (CARS) can take place in polycrystalline and opaque media [9]. The observation of wave localization, whether reduced, enhanced or simply tested by nonlinear processes, definitely opens new perspectives [10–14].

The temporal dimension is generally absent from these works. Indeed the scattered light emerges from the sample in close synchrony with the incoming field, either because one operates far from the absorption lines, or because the lifetime of the material resonances does not exceed the driving pulse duration, such as in CARS. The signature of the investigated signal is obtained either in the angular scattering pattern or in the emission spectrum, the latter applying to non-degenerate wave-mixing processes.

Instead, we now consider a nonlinear signal that emerges from the sample long after the extinction of the driving pulses. That time-domain discrimination may prove helpful in situations where neither the direction nor the wavelength would enable to select the relevant scattered emission. This time-delayed signal is produced by photon echo [15, 16], a nonlinear process that belongs to the same four-wave mixing (FWM) class as CARS [17]. Photon echo results from the resonant excitation of an absorbing line. The available time delay is only limited by the optical dipole lifetime  $T_2$  and may outdo the driving pulse duration by orders of magnitude.

Routinely used for  $T_2$  measurement, a photon echo experiment is usually performed in samples of high optical

quality. However there is considerable practical interest to substitute a cheap and easily produced rough powder to a high quality mono-crystal since interesting chemical solids are often difficult to crystallize [18]. Such a simplified access to  $T_2$  may expedite new compound selection in the prospect of classical and quantum processing [19–22].

The experimental observation of photon echo in rare earth ion doped polycrystalline powders at liquid helium temperature [23], and the successful demonstration of new compound testing [24], call for a better understanding of the scattered signal generation in such unusual conditions. In these studies, the echo is efficiently detected by heterodyne mixing with a replica of one driving field. Hence, quite unexpectedly, two distinct fields are able to preserve a strong correlation after erratic propagation through a disordered material although the corresponding speckle patterns look very different. The origin of such a disturbing and non intuitive feature must be clarified. The present paper extends the well-established linear multiple scattering theory to the non-linear, photon echo process. Special attention is paid to explaining the strong correlation of the echo with the driving field.

The manuscript is organized as follows: in Sec. II we summarize the main characteristics of photon echoes. In Sec. III we consider the case of a strongly disordered powder and we derive a physical model to take into account photon echoes in such a material. In Sec. IV theoretical expressions for the average driving fields and intensities are obtained. The theory is then expanded for the echo signal (average field, average intensity and correlation with a driving field) in Sec. V. Then we compare the analytical results with numerical simulations in Sec. VI before concluding in Sec. VII.

## II. PHOTON ECHO FEATURES

Photon echo [15, 16] refers to the time-delayed nonlinear coherent optical response to resonant excitation by a specific sequence of light pulses.

In absorbing materials,  $T_2$ , the optical dipole lifetime, may be much larger than the inverse absorption bandwidth. Indeed that bandwidth may reflect the Doppler shift, in gases, or a non-uniform transition fre-

---

\* romain.pierrat@espci.fr

quency shift, caused by interaction with the environment, in condensed matter, rather than the homogeneous linewidth. This quasi-static effect is known as inhomogeneous broadening. When resonantly excited by a light pulse much shorter than  $T_2$ , the optical dipole radiates a free induction decay (FID) signal. However this emission rapidly fades out because of inhomogeneous phase shift, although optical dipoles keep on oscillating in the medium. The photon echo process, closely related to spin echo in Nuclear Magnetic Resonance (NMR), is used to cancel the inhomogeneous phase shift and to recover a radiative signature of the surviving dipoles.

Let us focus on stimulated echoes [25], generated by a sequence of three successive pulses that resonantly excite an ensemble of two-level atoms. The pulses are labeled 1, 2 and 3, according to their time order. By reducing the level population difference, resonant excitation partially bleaches the material over the pulse bandwidth. However, bleaching caused by time-separated pulses is not uniform over the excitation bandwidth. In the same way as, in space domain, two *angled* beams can imprint a diffraction grating on a photographic plate, a pair of *time separated* pulses spectrally modulates the level population difference. Hence, pulses 1 and 2, separated by time interval  $t_{12}$ , modulate the bleaching with period  $1/t_{12}$ . Then, in the same way as a spatial grating deflects a probe beam at an angle determined by the inverse ridge spacing, the spectral grating delays the response to pulse 3, acting as a probe. The response delay equals  $t_{12}$ , the inverse period of the bleaching spectral modulation.

In order to express an oscillating dipole in terms of the driving pulses, let us define the positive and negative frequency components of the  $i$ -labeled driving field  $E_i(\mathbf{r}, t)$ , centered at time  $t_i$ , as

$$E_i(\mathbf{r}, t) = \frac{1}{2} [\mathcal{A}_i(\mathbf{r}, t) \exp(i\omega_L t) + \text{c.c.}] \quad (1)$$

$$= \frac{1}{2} [\mathcal{E}_i(\mathbf{r}, t - t_i) + \text{c.c.}] \quad (2)$$

where  $\omega_L$  represents the pulse central frequency. Interaction with an optical dipole is characterized by the Rabi frequency:

$$\Omega_i(\mathbf{r}, t) = \frac{\mu_{ab} \mathcal{E}_i(\mathbf{r}, t)}{\hbar} \quad (3)$$

where  $\mu_{ab}$  stands for the transition dipole moment. We also need the time-to-frequency Fourier transform of the Rabi frequency, defined as

$$\tilde{\Omega}_i(\mathbf{r}, \omega) = \int \Omega_i(\mathbf{r}, t) \exp[-i\omega t] dt. \quad (4)$$

This quantity is a dimensionless number and  $|\tilde{\Omega}_i^*(\mathbf{r}, \omega_L)|$  represents the pulse area. Since, according to Eq. (1),  $\Omega_i(\mathbf{r}, t)$  is centered at  $t = 0$ ,  $\tilde{\Omega}_i(\mathbf{r}, \omega)$  is a slowly varying function of  $\omega$  over the pulse bandwidth.

In the weak field limit, when  $|\tilde{\Omega}_i^*(\mathbf{r}, \omega_L)| \ll 1$ , the dipole  $d(\mathbf{r}, \omega_{ab}, t)$ , oscillating at position  $\mathbf{r}$  at frequency

$\omega_{ab}$ , can be expressed to lowest order in the three driving fields as [17]

$$d(\mathbf{r}, \omega_{ab}, t) = i \frac{\mu_{ab}}{4} \exp \left[ -\frac{t - t_3 + t_{12}}{T_2} - \frac{t_{23}}{T_1} \right] \\ \times \left\{ \tilde{\Omega}_1^*(\mathbf{r}, \omega_{ab}) \tilde{\Omega}_2(\mathbf{r}, \omega_{ab}) \tilde{\Omega}_3(\mathbf{r}, \omega_{ab}) \exp [i\omega_{ab} (t - t_3 - t_{12})] \right. \\ \left. - \text{c.c.} \right\} \quad (5)$$

where  $T_1$  represents the upper level lifetime. At time  $t = t_3 + t_{12}$  all the dipoles, irrespective of the transition frequency value, are phased back together since  $\omega_{ab} (t - t_3 - t_{12})$  vanishes, which results in the photon echo emission. Since the oscillating dipole at  $\mathbf{r}$  is expressed in terms of the fields at the same position, with no additional space dependence, this description applies not only to transparent, high optical quality media, but also to scattering materials.

Similar expressions describe the various optical four-wave mixing processes. An important difference deserves to be noticed, which is the absence of contribution proportional to  $\tilde{\Omega}_1(\mathbf{r}, \omega_{ab}) \tilde{\Omega}_2^*(\mathbf{r}, \omega_{ab}) \tilde{\Omega}_3(\mathbf{r}, \omega_{ab})$ . The extinction of this term is not related to any spatial phase matching condition but instead reflects causality [17].

### III. PHYSICAL MODEL FOR PHOTON ECHOES IN DISORDERED MATERIALS

#### A. Structure of the medium

The polycrystalline powder in which photon echo has been observed [23] can be sketched as an ensemble of contiguous, disorderly distributed, microscopic grains that contain the active echo-generating material [Fig. 1 (a)]. Successive reflection and refraction processes at the grain-walls result in the observed multiple scattering effect.

Such a disordered succession of index-steps is difficult to model. Instead, we propose a much simpler scheme that preserves the two leading features, namely echo generation and multiple scattering. We replace the original structure by (1) an echo-generating continuous and homogeneous active medium, with (2) randomly embedded point-scatterers. This model is illustrated in Fig. 1 (b). One can switch from the disordered sample to the corresponding homogeneous slab by just removing the scatterers. This offers an easy way to compare the signals in these two situations.

Moreover, to achieve large optical thickness numerically, we consider a two dimensional system and scalar waves (i.e. the electric field is oriented along the translational invariant direction  $y$ ) embedded in a slab geometry with size  $L$  along  $z$  and infinite along  $x$  as shown in Fig. 1. Translational invariance along  $y$  results in substituting the point scatterers with  $N_s$  rectilinear, infinitely long, thin rods, randomly placed inside the system at positions

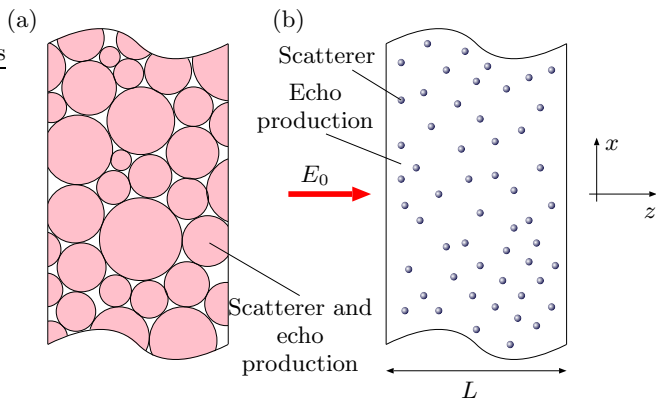


Figure 1. (a) Sketch of the experimentally investigated system, composed of assembled crystalline grains. (b) Model used in the theoretical and numerical studies. In the echo-generating continuous homogeneous medium, point scatterers are immersed at random, which gives rise to the multiple scattering effect. The particles are lying in a slab geometry of size  $L$  which is convenient to derive simple analytical expressions.

$r_j$ . With transverse size much smaller than the optical wavelength, the rods are assumed to behave as isotropic scatterers. In addition, light is scattered elastically, without absorption in the rods. This simplified model does not permit a quantitative comparison with the experiment of Ref. 23 but contains all physical ingredients (scattering and echo production) required to give physical insights into the existence of the strong correlation between the driving fields and the echo beam.

## B. Coupled wave equations

Let  $E^{(1,2,3)}(\mathbf{r}, \omega)$  denote the three driving field spectral amplitudes, at position  $\mathbf{r}$  and frequency  $\omega$ . One also defines the exciting field  $E_{\text{exc}}^{(1,2,3)}(\mathbf{r}_i, \omega)$  at rod position  $\mathbf{r}_i$ . The latter corresponds to the field illuminating the scatterer, and is obtained by subtracting the scatterer emission from the total field. The wave equation reads [3]

$$E_{\text{exc}}^{(1,2,3)}(\mathbf{r}_i, \omega) = E_0(\mathbf{r}_i, \omega) + k_0^2 \alpha \sum_{\substack{j=1 \\ j \neq i}}^{N_s} G_0(\mathbf{r}_i - \mathbf{r}_j, \omega) E_{\text{exc}}^{(1,2,3)}(\mathbf{r}_j, \omega), \quad (6)$$

where  $k_0 = \omega/c$  is the wave vector in vacuum,  $\alpha$  represents the scatterer polarizability, and  $G_0$  is the free space Green function, connecting the field  $E$  at any position inside the system to an electric-dipole point source  $p$  lying at position  $\mathbf{r}_0$  by

$$E(\mathbf{r}, \omega) = \mu_0 \omega^2 G_0(\mathbf{r} - \mathbf{r}_0, \omega) p. \quad (7)$$

In a 2D scalar problem,  $G_0$  is given by the isotropic function

$$G_0(\mathbf{r} - \mathbf{r}_0, \omega) = \frac{i}{4} H_0^{(1)}(k_0 |\mathbf{r} - \mathbf{r}_0|) \quad (8)$$

where  $H_0^{(1)}$  denotes the Hankel function of first kind and zero order.

In elastic, isotropic, scattering conditions, energy conservation leads to

$$k_0 \text{Im} \alpha = \frac{k_0^3}{4} |\alpha|^2 \quad (9)$$

where the left-hand and right-hand sides, respectively, represent the extinction and scattering cross sections [1–3]. Therefore, the cross section cannot exceed  $4/k_0$ , which corresponds to

$$\alpha = \alpha_{\text{max}} = \frac{4i}{k_0^2} \quad (10)$$

For the sake of simplicity, one derives the three driving fields from identical incident fields, denoted as  $E_0$ , and given by plane waves at normal incidence

$$E_0(\mathbf{r}, \omega) = E_0 \exp[ik_0 z]. \quad (11)$$

Once the exciting fields are known, the electric driving fields can be calculated at any position inside or outside the medium thanks to the relation

$$E^{(1,2,3)}(\mathbf{r}, \omega) = E_0(\mathbf{r}, \omega) + k_0^2 \alpha \sum_{j=1}^{N_s} G_0(\mathbf{r} - \mathbf{r}_j, \omega) E_{\text{exc}}^{(1,2,3)}(\mathbf{r}_j, \omega). \quad (12)$$

The echo is created by active atoms placed inside the host medium. In the previous section, we have established that the source of the echo beam is given by  $\tilde{\Omega}_1^*(\mathbf{r}, \omega_{ab}) \tilde{\Omega}_2(\mathbf{r}, \omega_{ab}) \tilde{\Omega}_3(\mathbf{r}, \omega_{ab})$ . Thus, the electric field of the echo signal can be cast in the form

$$E_{\text{exc}}^{(4)}(\mathbf{r}_i, \omega) = k_0^2 \chi \int G_0(\mathbf{r}_i - \mathbf{r}', \omega) E^{(1)*}(\mathbf{r}', \omega) \times E^{(2)}(\mathbf{r}', \omega) E^{(3)}(\mathbf{r}', \omega) d\mathbf{r}' + k_0^2 \alpha \sum_{\substack{j=1 \\ j \neq i}}^{N_s} G_0(\mathbf{r}_i - \mathbf{r}_j, \omega) E_{\text{exc}}^{(4)}(\mathbf{r}_j, \omega). \quad (13)$$

where  $\chi$  is a constant describing the coupling between the driving fields and the echo beam. Exactly as for the driving fields, the electric field of the echo at any position can be deduced from the relation

$$E^{(4)}(\mathbf{r}, \omega) = k_0^2 \chi \int G_0(\mathbf{r} - \mathbf{r}', \omega) E^{(1)*}(\mathbf{r}', \omega) \times E^{(2)}(\mathbf{r}', \omega) E^{(3)}(\mathbf{r}', \omega) d\mathbf{r}' + k_0^2 \alpha \sum_{j=1}^{N_s} G_0(\mathbf{r} - \mathbf{r}_j, \omega) E_{\text{exc}}^{(4)}(\mathbf{r}_j, \omega). \quad (14)$$

This set of equations is overall reminiscent of previous descriptions of non-linearities in complex systems [13, 26–28], and similarities with these works will be found all along the following theory.

For a given spatial distribution of the  $N_s$  scatterers, referred to as a *configuration*, one has to solve the  $N_s$ -linear-equation-set represented by Eq. (6). Then, with the help of Eq. (12), one can calculate the source term in Eq. (13), which leads to the  $N_s$  values of the exciting echo field  $E_{\text{exc}}^{(4)}(\mathbf{r}_j, \omega)$ . Finally, substitution of  $E_{\text{exc}}^{(4)}(\mathbf{r}_j, \omega)$  into Eq. (14) determines the echo field anywhere, inside or outside the sample. The large size of the system linear equations can be handled only through numerical computation.

### C. Configurational average

The available experimental data are generally insufficient to define a specific configuration. Conversely, the detailed field structure, as provided by the numerical solution, often exceeds the detector spatial, angular, or temporal resolution. Therefore the experimentally accessible data, averaged over space and angle (in a rigid sample), or time (in a fluid), are expected to coincide with statistical averages over all possible disordered configurations. Of course, averaging washes out fine details, such as the speckle pattern of a fluctuating intensity emerging from a disordered medium.

One can approach the statistical average numerically, by averaging the solutions over a set of different configurations. More interestingly, in contrast with the single configuration problem, statistical average is accessible analytically. As will become clear in the following, the analytical solution not only saves computation time, but also brings physical insight into the observable quantities.

In the next two sections we shall adapt the available tools to echo generation in disordered media. The numerical solution, discussed in Sec. VI, will serve to validate the analytical procedure.

## IV. THE MULTIPLE SCATTERING THEORY FOR THE DRIVING FIELDS

In this section, we derive the average amplitude and intensity of the driving fields, as well as another quantity called the ladder operator, in order to get the necessary building blocks to obtain the echo signal. Since this is a textbook formalism, we only summarize the key steps. The interested reader may refer to Refs. 29 and 30 to find more details.

### A. Average field

Let us first compute the average field. For that purpose, we combine Eqs. (6) and (12) to obtain a cluster expansion of the driving fields. Omitting the exponents (1, 2, 3) and the frequency  $\omega$  related to the driving fields

for the sake of simplicity, we get [31]

$$E(\mathbf{r}) = E_0(\mathbf{r}) + k_0^2 \alpha \sum_{i=1}^{N_s} G_0(\mathbf{r} - \mathbf{r}_i) E_0(\mathbf{r}_i) + k_0^2 \alpha \sum_{i=1}^{N_s} G_0(\mathbf{r} - \mathbf{r}_i) k_0^2 \alpha \sum_{\substack{j=1 \\ j \neq i}}^{N_s} G_0(\mathbf{r}_i - \mathbf{r}_j) E_0(\mathbf{r}_j) + \dots \quad (15)$$

Averaging Eq. (15) over the configurations of the disorder leads to a closed and exact equation called the Dyson equation [32, 33]. In the following, the discussion is restricted to the Independent Scattering Approximation (ISA), where all the scattering events along a scattering sequence are statistically independent. The ISA is valid in a dilute medium, and the corresponding condition will be elucidated soon. In this limit, Dyson equation reads as

$$\langle E(\mathbf{r}) \rangle = E_0(\mathbf{r}) + \rho_s k_0^2 \alpha \int G_0(\mathbf{r} - \mathbf{r}') \langle E(\mathbf{r}') \rangle d\mathbf{r}' \quad (16)$$

where the brackets  $\langle \dots \rangle$  denote the statistical average and  $\rho_s$  is the density of scatterers.

Formal iterative solution of Eq. (16) leads to

$$\langle E(\mathbf{r}) \rangle = E_0(\mathbf{r}) + \rho_s k_0^2 \alpha \int \langle G(\mathbf{r} - \mathbf{r}') \rangle E_0(\mathbf{r}') d\mathbf{r}' \quad (17)$$

where

$$\langle G(\mathbf{r} - \mathbf{r}_0) \rangle = G_0(\mathbf{r} - \mathbf{r}_0) + \rho_s k_0^2 \alpha \int G_0(\mathbf{r} - \mathbf{r}') \langle G(\mathbf{r}' - \mathbf{r}_0) \rangle d\mathbf{r}'. \quad (18)$$

Hence, Eq. (17) expresses  $\langle E(\mathbf{r}) \rangle$  in terms of  $E_0$  and of the average Green function  $\langle G \rangle$ , which can be obtained by solving Eq. (18). Actually, Eq. (18) is the Dyson equation for the average Green function  $\langle G(\mathbf{r} - \mathbf{r}_0) \rangle$ , the average field radiated at position  $\mathbf{r}$  by a point source, located at  $\mathbf{r}_0$ .

To solve Eq. (18) we assume a bulk geometry, ignoring the finite size of the actual slab. In this framework, Fourier transforming Eq. (18) leads to:

$$\langle G(\mathbf{k}) \rangle = G_0(\mathbf{k}) + G_0(\mathbf{k}) \rho_s k_0^2 \alpha \langle G(\mathbf{k}) \rangle. \quad (19)$$

Substituting the Fourier transform of the free-space Green function

$$G_0(\mathbf{k}) = (k^2 - k_0^2)^{-1} \quad (20)$$

into Eq. (19), we readily get

$$\langle G(\mathbf{k}) \rangle = (k^2 - k_{\text{eff}}^2)^{-1}. \quad (21)$$

where

$$k_{\text{eff}} = k_0 \sqrt{1 + \rho_s \alpha}. \quad (22)$$

Except for the substitution of  $k_0$  with  $k_{\text{eff}}$ ,  $G_0(\mathbf{k})$  and  $\langle G(\mathbf{k}) \rangle$  are expressed in the same way. As a consequence, inverse Fourier transform of Eq. (21) leads to

$$\langle G(\mathbf{r} - \mathbf{r}_0) \rangle = \frac{i}{4} H_0^{(1)}(k_{\text{eff}}|\mathbf{r} - \mathbf{r}_0|), \quad (23)$$

which can be compared to the vacuum counterpart given by Eq. (8). The average field propagates in an effective system with an effective permittivity, the imaginary part of which describes the attenuation due to scattering (loss by scattering). Indeed

$$k_{\text{eff}} \sim k_0 + \frac{i}{2\ell} \quad (24)$$

where the scattering mean-free path  $\ell$  (average distance between two consecutive scattering events) is given by

$$1/\ell = \rho_s k_0 \text{Im } \alpha. \quad (25)$$

At this stage we are able to explicit the ISA condition in a dilute system as  $k_0 \ell \gg 1$ .

In the slab geometry, under illumination by a plane wave  $E_0(z)$  at normal incidence to the interfaces, Eq. (17) reduces to

$$\langle E(z) \rangle = E_0(z) + (k_{\text{eff}}^2 - k_0^2) \int_0^L \langle G(z - z') \rangle E_0(z') dz' \quad (26)$$

where

$$\langle G(z) \rangle = \frac{i}{4} \int_{-\infty}^{\infty} H_0^{(1)}(k_{\text{eff}} \sqrt{x^2 + z^2}) dx \quad (27)$$

$$= \frac{i}{2k_{\text{eff}}} \exp[ik_{\text{eff}}|z|] \quad (28)$$

is the 1D average Green function.

Substituting  $E_0(z)$  given by Eq. (11) into Eq. (26), one readily obtains:

$$\langle E(z) \rangle = E_0 \exp[ik_{\text{eff}}z] \quad (29)$$

in the ISA conditions.

The corresponding intensity (often called ballistic or coherent intensity) is given by

$$I_B(z) = |\langle E(z) \rangle|^2 = I_0 \exp\left[-\frac{z}{\ell}\right]. \quad (30)$$

From this, one can define the optical thickness as the ratio  $b = L/\ell$ , in terms of which the relative power, ballistically transmitted by the system, can be expressed as  $T_B = \exp(-b)$ .

It is usual in the multiple scattering theory to have a simple representation of iterative equations in terms of diagrams. For Eq. (18), it reads

$$\langle G(\mathbf{r} - \mathbf{r}_0) \rangle = \text{---} + \text{---} \circ \text{---} + \text{---} \circ \text{---} \circ \text{---} + \dots \quad (31)$$

where circles and solid lines denote scattering events and free-space Green functions  $G_0$  respectively.

## B. Average intensity

The same work can be carried out to compute the average intensity. The field correlation  $\langle E(\mathbf{r})E^*(\boldsymbol{\rho}) \rangle$ , coinciding with the average intensity when  $\mathbf{r} = \boldsymbol{\rho}$ , is driven by the Bethe-Salpeter equation [34, 35], which, in the dilute system approximation, reduces to

$$\langle I(\mathbf{r}) \rangle = |\langle E(\mathbf{r}) \rangle|^2 + \frac{4k_0}{\ell} \int |\langle G(\mathbf{r} - \mathbf{r}') \rangle|^2 \langle I(\mathbf{r}') \rangle d\mathbf{r}'. \quad (32)$$

The iterative solution to that equation can be expanded as a series of diagrams:

$$\langle I(\mathbf{r}) \rangle = \text{---} + \text{---} \circ \text{---} + \text{---} \circ \text{---} \circ \text{---} + \dots \quad (33)$$

where the upper (lower) line corresponds to the field (its conjugate) respectively. Thick solid lines correspond to the average Green functions and thick dashed lines denote average fields. The circles represent the scattering events, which are joined by vertical lines since they occur at the same position, in the same order, for both fields. The resulting characteristic shape is known as a ladder diagram.

Not only does that diagram expansion represent a convenient mathematical tool, but it also conveys a physical picture for the averaged intensity propagation through a disordered medium. Indeed, as illustrated by this diagram, statistical average washes out most of the contributions to  $\langle I \rangle$  at position  $\mathbf{r}$  – those affected by the erratic spatial phase factors that build up when  $E$  and  $E^*$  follow different paths, and strongly depend on the path details. Only survive the scattering sequences where both fields  $E$  and  $E^*$  follow the same path, with the same scatterers located at the same positions. As it will soon become clear, that drastic selection results in speckle structure erasure. Averaging over a spatial region, with volume larger than  $\lambda^3$ , for a given and fixed scatterer distribution, is expected to achieve the same scattering path selection as statistical averaging over scatterer distributions.

With the help of the ballistic intensity defined in Eq. (30), one readily casts Eq. (32) in the form

$$I_D(\mathbf{r}) - \frac{4k_0}{\ell} \int |\langle G(\mathbf{r} - \mathbf{r}') \rangle|^2 I_D(\mathbf{r}') d\mathbf{r}' = \frac{4k_0}{\ell} \int |\langle G(\mathbf{r} - \mathbf{r}') \rangle|^2 I_B(\mathbf{r}') d\mathbf{r}'. \quad (34)$$

where  $I_D(\mathbf{r}) = \langle I(\mathbf{r}) \rangle - I_B(\mathbf{r})$  represents the diffuse intensity. Deep inside the medium, at distances  $\gg \ell$  from the interfaces,  $|\langle G(\mathbf{r} - \mathbf{r}') \rangle|^2$  is given by Eq. (23). In this region, one may simplify the left-hand side of Eq. (34), observing that the spatial frequency spectrum of  $I_D(\mathbf{r})$  is much narrower than that of  $|\langle G(\mathbf{r} - \mathbf{r}') \rangle|^2$ . Hence one

may replace the latter function Fourier transform by its second order Taylor expansion, which leads to

$$I_D(\mathbf{r}) - \frac{4k_0}{\ell} \int |\langle G(\mathbf{r} - \mathbf{r}') \rangle|^2 I_D(\mathbf{r}') d\mathbf{r}' = -\frac{\ell^2}{2} \Delta I_D(\mathbf{r}) \quad (35)$$

The right-hand side in Eq. (34), operating as a source term, vanishes far from the interfaces, in the region where Eq. (23) is valid. Hence, according to Eq. (35), Eq. (34) reduces to  $\Delta I_D(\mathbf{r}) = 0$ , which conveys no information on  $I_D(\mathbf{r})$  build-up from ballistic intensity. Closer to the input interface, the source term no longer vanishes but the bulk approximation, ignoring the finite size of the slab, no longer applies. However, numerical simulations appear to be consistent with Eq. (35), provided the right-hand side of this equation is replaced with  $I_B(\mathbf{r})$ .

The resulting diffusion equation [30], now considered to be valid throughout the medium, reads as

$$-\frac{\ell^2}{2} \Delta I_D(\mathbf{r}) = I_B(\mathbf{r}). \quad (36)$$

That equation is complemented by two boundary conditions, assessing the absence of incoming diffuse intensity through both interfaces:

$$I_D(z=0) - z_0 \left. \frac{\partial I_D(z)}{\partial z} \right|_{z=0} = 0, \quad (37)$$

$$I_D(z=L) + z_0 \left. \frac{\partial I_D(z)}{\partial z} \right|_{z=L} = 0, \quad (38)$$

where  $z_0$ , the so called extrapolation length [36], is on the order of  $\ell$ . Let  $F(z)$  represent any solution of equation

$$\frac{\ell^2}{2} F''(z) = I_0 \exp\left[-\frac{z}{\ell}\right]. \quad (39)$$

Then, the solution of the diffusion equation, consistent with the boundary conditions, reads

$$I_D(z) = \frac{(z+z_0)F(L) + (L+z_0-z)F(0)}{L+2z_0} + \frac{z_0(z+z_0)F'(L) - z_0(L+z_0-z)F'(0)}{L+2z_0} - F(z). \quad (40)$$

Finally the solution of Eq. (36) reads

$$I_D(z) = 2I_0 \left[ \left(1 + \frac{z_0}{\ell}\right) \frac{L+z_0-z}{L+2z_0} - \exp\left(-\frac{z}{\ell}\right) \right]. \quad (41)$$

The factor  $z_0/\ell$  in this equation makes  $I_D(z)$  sensitive to  $z_0$  at any depth in the medium.

The variations of  $I_B$  and  $I_D$  with  $z$  are plotted in Fig. 2. We have taken  $z_0 = \pi\ell/4$ , a standard value for a 2D problem [30]. We may notice the very fast decay of  $I_B$  on a typical length given by  $\ell$ , and the slower decay of  $I_D$ . This plot represents a stationary state, where the

sample, continuously fed by the incident plane wave, re-emits all that energy through the interfaces. Although Eq. (41) is valid only within the slab boundaries, the spatial intensity distribution, as represented in Fig. 2, suggests that most of the incoming flux is scattered in backward direction through the input interface.

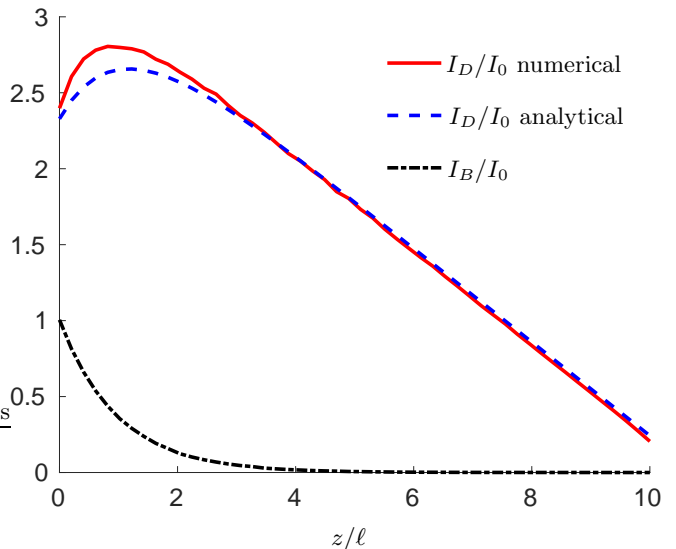


Figure 2. (Color online) Ballistic ( $I_B$ , black dash-dotted line) and diffuse ( $I_D$ , blue dashed line and red solid line) intensity as a function of the depth  $z$  inside the slab for  $b = 10$  and  $k\ell = 40$ .

According to Eqs. (30) and (41), the average intensity reads

$$\langle I(z) \rangle = I_0 \left[ 2 \left(1 + \frac{z_0}{\ell}\right) \frac{L+z_0-z}{L+2z_0} - \exp\left(-\frac{z}{\ell}\right) \right]. \quad (42)$$

### C. Ladder operator

In the same way as we have defined the average Green function for the average field, we may define a Green function for the average intensity. Called the ladder operator, this quantity can be represented by the diagram

$$L(\mathbf{r}, \mathbf{r}_0) = \begin{array}{c} \circ \\ | \\ \circ \end{array} + \begin{array}{c} \circ \text{---} \circ \\ | \quad | \\ \circ \text{---} \circ \end{array} + \begin{array}{c} \circ \text{---} \circ \text{---} \circ \\ | \quad | \quad | \\ \circ \text{---} \circ \text{---} \circ \end{array} + \dots \quad (43)$$

which analytically gives

$$L(\mathbf{r}, \mathbf{r}_0) = \frac{4k_0}{\ell} \delta(\mathbf{r} - \mathbf{r}_0) + \frac{4k_0}{\ell} \int |\langle G(\mathbf{r} - \mathbf{r}') \rangle|^2 L(\mathbf{r}', \mathbf{r}_0) d\mathbf{r}'. \quad (44)$$

In large systems ( $L \gg \ell$ ), Eq. (44) reduces to

$$-\frac{\ell^2}{2} \Delta L(\mathbf{r}, \mathbf{r}_0) = \frac{4k_0}{\ell} \delta(\mathbf{r} - \mathbf{r}_0). \quad (45)$$

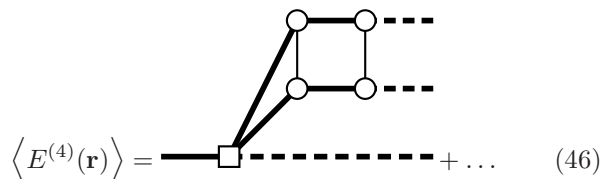
Expressed in terms of  $|G(\mathbf{r} - \mathbf{r}')|^2$ , just as Eq. (32), the ladder operator does not help to handle source terms such as  $I_B(\mathbf{r})$ , which are strongly confined to the close vicinity of the interfaces. However, as will be seen soon, it proves helpful to deal with slowly varying sources terms, spreading all over the medium.

## V. THE MULTIPLE SCATTERING THEORY FOR THE ECHO SIGNAL

This section is the original part of the study. We intend to analytically derive the statistical average of the echo field and intensity and to express the echo field correlation with one of the driving fields. According to Ref. 23, the amplitude of this correlation can be large, even in the multiple scattering regime. The following derivation will help to understand the origin of this strong correlation.

### A. Average echo field

Along the lines of the above summarized multiple scattering theory, we have to identify the most important diagrams in the context of photon echo physics. Let us focus first on the average echo field. According to Eqs. (13) and (14), the echo signal is created at any position in the host medium and is given by  $E^{(1)*}(\mathbf{r}', \omega)E^{(2)}(\mathbf{r}', \omega)E^{(3)}(\mathbf{r}', \omega)$ . To construct the average echo field, we let the average intensity and the average field merge at  $\mathbf{r}'$ . The resulting signal propagation from  $\mathbf{r}'$  to  $\mathbf{r}$  is carried out by the average Green function. That scheme is represented by the following diagram structure:



$$\langle E^{(4)}(\mathbf{r}) \rangle = \text{---} \square \text{---} \text{---} + \dots \quad (46)$$

where the square represents echo generation; the middle line corresponds to  $E^{(1)*}$ ; the upper and lower lines may respectively refer to  $E^{(2)}$  and  $E^{(3)}$ , or to  $E^{(3)}$  and  $E^{(2)}$ . All the significant contributions to  $\langle E^{(4)}(\mathbf{r}) \rangle$  share the same structure, with different numbers of scattering events on each branch. Due to the possible permutation of  $E^{(2)}$  and  $E^{(3)}$ , each diagram should be counted twice.

Finally, in quite the same way as the incident average field [see Eq. (26)],  $\langle E^{(4)}(\mathbf{r}) \rangle$  can be expressed analytically as follows:

$$\langle E^{(4)}(z) \rangle = 2k_0^2 \chi \int_0^L \langle G(z - z') \rangle \langle I(z') \rangle \langle E(z') \rangle dz', \quad (47)$$

still in a dilute system with  $k_0 \ell \gg 1$ . In the large optical thickness limit, with  $b \gg 1$ , the integral upper bound can be changed into  $z$ , without significant deviations except

at the very beginning of the slab ( $z < \ell$ ). Using Eqs. (29) and (42), we finally get

$$\begin{aligned} \langle E^{(4)}(z) \rangle &= ik_0 \ell \chi E_0 I_0 \exp[ik_{\text{eff}} z] \\ &\times \left\{ \frac{2}{\ell} \left(1 + \frac{z_0}{\ell}\right) \frac{(L + z_0)z - z^2/2}{L + 2z_0} + \exp\left[-\frac{z}{\ell}\right] - 1 \right\}. \end{aligned} \quad (48)$$

In terms of intensity, this gives

$$I_B^{(4)}(z) = \left| \langle E^{(4)}(z) \rangle \right|^2. \quad (49)$$

These quantities can be compared with their equivalents in a homogeneous slab with the same active atom concentration. To deprive the slab from all the scattering centers, we just replace the average Green function, intensity and field in Eq. (47) by their counterparts for an homogeneous medium, which gives:

$$E_{\text{hom}}^{(4)}(z) = k_0^2 \chi \int_0^L G_0(z - z') I_0(z') E_0(z') dz'. \quad (50)$$

Provided  $k_0 z \gg 1$ , the corresponding homogeneous echo field and intensity reduce to:

$$E_{\text{hom}}^{(4)}(z) = \frac{ik_0 \chi E_0 I_0 z}{2} \exp[ik_0 z], \quad (51)$$

$$\text{and } I_{\text{hom}}^{(4)}(z) = \frac{k_0^2 \chi^2 I_0^3 z^2}{4}. \quad (52)$$

It should be pointed out that the bulk geometry approximation we have been using, imposing the large optical depth condition  $L \gg \ell$ , forbids any continuous transition from a disordered to a homogeneous medium, for example by continuously increasing the scattering mean free path  $\ell$ .

In Fig. 3, we have plotted  $I_B^{(4)}(z)$  and  $I_{\text{hom}}^{(4)}(z)$ , both normalized to  $I_{\text{hom}}^{(4)}(L)$ , the echo intensity at the exit interface of a homogeneous slab. Close to the input,  $I_B^{(4)}(z)$  and  $I_{\text{hom}}^{(4)}(z)$  exhibit the same parabolic variation with  $z$ , which is the signature of spatially coherent buildup of the echo grows. In that region, the much faster growth of echo intensity in the disordered medium reflects the incident energy confinement near the input side of the slab. However, while the signal intensity grows quadratically in the homogeneous slab, a maximum is reached at  $z \simeq 2\ell$  in the disordered medium, followed by a fast decrease with  $z$ . Scattering affects both the echo generation and propagation. On the one hand, the driving field  $\langle E(z) \rangle$  drops with  $z$ , reducing contributions to the signal deeper into the slab. On the other hand, the ballistic component of the echo is attenuated as it propagates through the medium, feeding its diffuse part.



with

$$\mathcal{K} = k_0^2 \chi \int \langle G(\mathbf{r}'' - \mathbf{r}''') \rangle \langle G^*(\mathbf{r}'' - \boldsymbol{\rho}) \rangle \times \langle G^*(\boldsymbol{\rho} - \mathbf{r}''') \rangle d\boldsymbol{\rho} d\mathbf{r}'''. \quad (59)$$

Making use again of Eq. (57), we can simplify  $\mathcal{K}$  into

$$\mathcal{K} = k_0 \ell \chi \int \text{Im} [\langle G(\boldsymbol{\rho}) \rangle] \langle G^*(\boldsymbol{\rho}) \rangle d\boldsymbol{\rho}, \quad (60)$$

which, for a dilute medium, reduces to

$$\mathcal{K} = \frac{k_0 \ell \chi}{2i} \int |\langle G(\boldsymbol{\rho}) \rangle|^2 d\boldsymbol{\rho} \quad (61)$$

$$= \frac{\ell^2 \chi}{2i} \text{Im} [\langle G(0) \rangle] = \frac{\ell^2 \chi}{8i}. \quad (62)$$

Applying the Laplace operator to Eq. (58), and making use of Eq. (45), one finally obtains

$$-\frac{\ell^2}{2} \Delta C_D^{(4)}(\mathbf{r}) = -ik_0 \ell \chi \langle I(\mathbf{r}) \rangle^2. \quad (63)$$

This equation is the main result from the analytical theory. It takes a similar form as Eq. (36) obtained above for the diffuse intensity. However, in sharp contrast to Eq. (36), the source term in Eq. (63) has significant values at any depth in the medium, which entails a twofold consequence. First, since the correlation buildup is not localized near the slab input, the bulk approximation made for the diffusion equation is justified. There is not need to try to extrapolate this equation outside its region of validity. Second, the continuous feeding of  $C_D^{(4)}(\mathbf{r})$  by  $\langle I(\mathbf{r}) \rangle^2$  strongly contributes to enhance the correlation, all along the progression through the medium.

Provided Eq. (63) is complemented with the boundary conditions [see Eq. (37)] previously used to solve Eq. (36), the solution  $C_D^{(4)}(z)$  is also given by Eq. (40), where  $F(z)$  now represents any solution of

$$F''(z) = -2i \frac{k_0}{\ell} \chi \langle I(z) \rangle^2. \quad (64)$$

We may compare the correlation in a disordered medium with the corresponding quantity in an homogeneous slab. The latter reads as

$$C_{\text{hom}}^{(4)}(z) = E_{\text{hom}}(z) E_{\text{hom}}^{(4)*}(z) = \frac{\chi I_0^2}{4} \{-2ik_0 z - 1 + \exp[-2ik_0(L - z)]\} \quad (65)$$

which, for depths larger than  $\lambda = 2\pi/k_0$ , becomes

$$C_{\text{hom}}^{(4)}(z) = \frac{-ik_0 \chi I_0^2 z}{2} = i \sqrt{I_0 I_{\text{hom}}^{(4)}(z)}. \quad (66)$$

According to Figs. 4 where we have displayed the variations of  $|C_D^{(4)}(z)| / |C_{\text{hom}}^{(4)}(L)|$  with  $z$ , the strength of  $|C_D^{(4)}(z)|$  largely exceeds that of  $|C_{\text{hom}}^{(4)}(L)|$  at any depth.

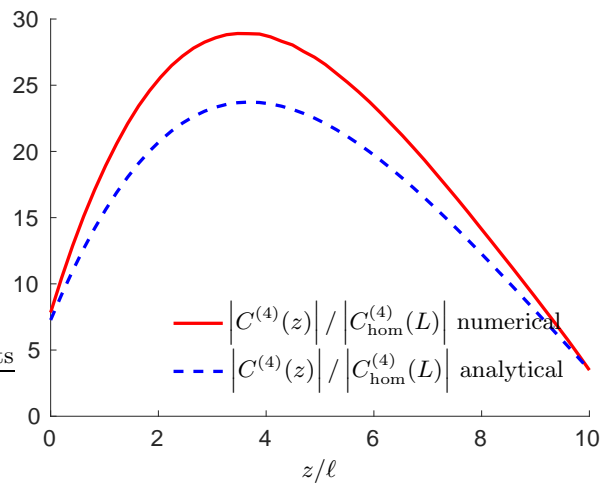


Figure 4. (Color online) Correlation of the echo signal with one of the driving fields  $C^{(4)} = \langle EE^{(4)*} \rangle$  as a function of the depth  $z/\ell$  inside the slab (analytical solution: blue dashed line; numerical computation: solid line);  $b = 10$  and  $k_0 \ell = 40$ . The correlation is normalized to the corresponding quantity at the exit of a homogeneous slab.

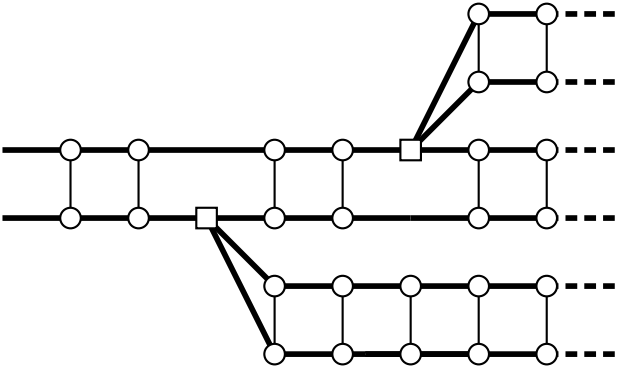
Normalization with  $\sqrt{\langle I \rangle \langle I^{(4)} \rangle}$ , where  $\langle I^{(4)} \rangle$  stands for the echo average intensity, helps to reveal the correlation strength. Indeed, as a consequence of the Cauchy Schwarz inequality, the variation range of  $|C_D^{(4)}(z)| / \sqrt{\langle I(z) \rangle \langle I^{(4)}(z) \rangle}$  is limited to interval  $[0, 1]$ , where the upper bound is reached when the echo is fully correlated with the reference field. In order to obtain the normalized correlation, we calculate the echo average intensity in the next section.

### C. Average intensity of the echo and normalized correlation

As for the incoming intensity and the calculation of the correlation function, we expand the echo average intensity into a ballistic and a diffuse part as follows:

$$\langle I^{(4)}(\mathbf{r}) \rangle = I_B^{(4)}(\mathbf{r}) + I_D^{(4)}(\mathbf{r}). \quad (67)$$

The ballistic part is given by Eq. (49) and the diffuse part reads diagrammatically as

$$I_D^{(4)}(\mathbf{r}) =$$


$$+ \dots \quad (68)$$

We follow the same procedure as for the echo correlation function  $C_D^{(4)}$ . According to the diagram, the source term for the echo diffuse intensity reads as the correlation multiplied by the average intensity. This leads to the following diffusion equation governing the evolution of  $I_D^{(4)}$ :

$$-\frac{\ell^2}{2}\Delta I_D^{(4)}(\mathbf{r}) = 2k_0\ell \operatorname{Re} \left[ i\chi^* C^{(4)}(\mathbf{r}) \right] \langle I(\mathbf{r}) \rangle. \quad (69)$$

Again, the source term in this diffusion equation is delocalized over the whole sample, thus leading to a different behavior for  $I_D^{(4)}$  compared to  $I_D$  (or for  $\langle I^{(4)} \rangle$  compared to  $\langle I \rangle$ ) even if both quantities have significant values for all depths inside the slab, as illustrated in Figs. 5 and 2.

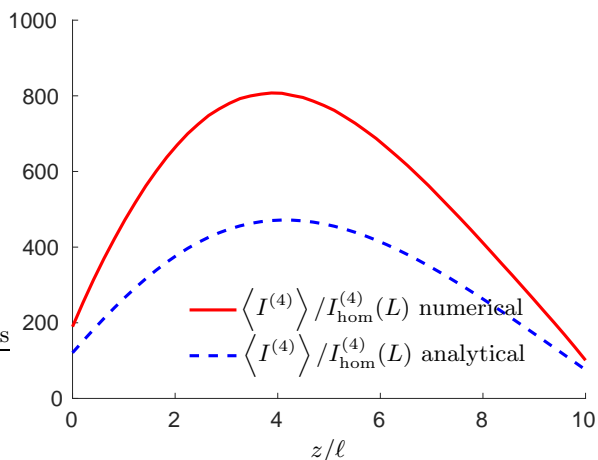


Figure 5. (Color online) Echo intensity  $\langle I^{(4)} \rangle = \langle |E^{(4)}|^2 \rangle$  as a function of the depth  $z/\ell$  inside the slab (numerical computation: red solid line; analytical solution: blue dashed line).  $b = 10$  and  $k_0\ell = 40$ .

We note that  $\langle I^{(4)} \rangle$  is much larger than  $I_{\text{hom}}^{(4)}$ . Two arguments can be put forward as an explanation. (1) In

a random walk picture, the paths followed by photons inside the disordered medium can be much longer than the slab thickness. Indeed, the average path length is of the order of  $\langle s \rangle = 2L^2/\ell$  in a thick ( $b \gg 1$ ) and dilute ( $k_0\ell \gg 1$ ) scattering medium while it is  $s_{\text{hom}} = L$  for an homogeneous slab. (2) In a disordered medium, the driving fields have larger values than in an homogeneous material thanks to light confinement by scattering. This is visible in Fig. 2 where a maximum average intensity on the order of  $2.5I_0$  is reached.

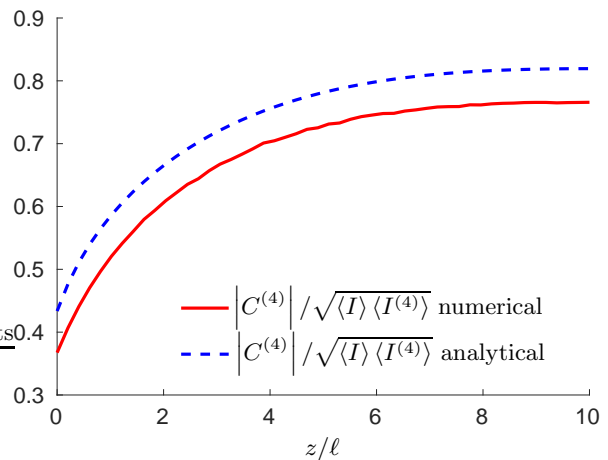


Figure 6. (Color online) Normalized correlation  $|C^{(4)}(z)| / \sqrt{\langle I(z) \rangle \langle I^{(4)}(z) \rangle}$  inside the slab. The analytical result, based on the diagrammatic approach, and the numerical computation are both displayed as a function of the normalized depth  $z/\ell$  (blue dashed line and red solid line respectively), with  $b = 10$  and  $k_0\ell = 40$ .

Finally, Fig. 6 shows the dramatic increase of the normalized correlation  $|C^{(4)}(z)| / \sqrt{\langle I(z) \rangle \langle I^{(4)}(z) \rangle}$  with the penetration depth, up to  $\approx 0.8$  at the slab exit.

## VI. NUMERICAL RESULTS

The analytical expressions are expected to be consistent with the statistically averaged solutions of the coupled wave equations (see Sec. III B). We must resort to numerical computation to obtain these solutions, in order to validate the analytical approach.

Solving Eqs. (6) represents the most challenging task. Indeed, to solve this set of  $N_s$  equations, one has to inverse a large  $N_s \times N_s$  matrix, the actual size of which is imposed by the large depth ( $L \gg \ell$ ) and slab geometry (infinite transverse extension) assumptions. In order to minimize  $N_s$ , we reduce the slab transverse dimension to  $D = 4L$ , expected to be a good trade-off, limiting finite-size effects while maintaining a reasonable computing time. To satisfy the diffusive-regime, large-depth, condition we set  $L/\ell = 10$ . Hence  $N_s = DL\rho_s = 400\ell^2\rho_s$ . According to Eq. (25), for a given value of  $\ell$ , the scat-

ter density  $\rho_s$  is minimized when  $\text{Im} \alpha$  is maximized. As already pointed out in Sec. III B (see Eq. (10)), the maximum value of  $\text{Im} \alpha$ , compatible with energy conservation, is  $4/k_0^2$ , which leads to  $\ell^2 \rho_s = k_0 \ell / 4$ . Finally, to satisfy the dilute medium condition  $k_0 \ell \gg 1$ , we set  $k_0 \ell = 40$ , which leads to  $N_s = 4000$ .

Since the echo signal Eqs. (13) and the driving field Eqs. (6) only differ from each other through the source term, they are both solved by the same inverse matrix. In the echo signal equations we have to discretize the integral of the source term. As we perform statistics (i.e. computation of average fields, intensities and correlations), we have chosen to treat the active region as a collection of  $N_a$  randomly placed active atoms at positions  $\boldsymbol{\rho}_j$ . This leads to

$$\begin{aligned} & k_0^2 \chi \int G_0(\mathbf{r} - \mathbf{r}') E^{(1)*}(\mathbf{r}') E^{(2)}(\mathbf{r}') E^{(3)}(\mathbf{r}') d\mathbf{r}' \\ & \sim k_0^2 \chi S_a \sum_{j=1}^{N_a} G_0(\mathbf{r} - \boldsymbol{\rho}_j) E^{(1)*}(\boldsymbol{\rho}_j) E^{(2)}(\boldsymbol{\rho}_j) E^{(3)}(\boldsymbol{\rho}_j) \end{aligned} \quad (70)$$

where  $S_a = LD/N_a$  is the surface of one active atom. The statistical observables are not sensitive to the number of active regions  $N_a$ , even if very small (i.e. continuum not reached). In practice, we have used  $N_a = 4000$ .

Having obtained the expression of the exciting echo field on each scatterer, we use Eq. (14) to compute the echo field at any position in or outside the system.

Repeating the same procedure for a large set of randomly drawn configurations, we are in position to evaluate statistical quantities such as the average echo field, the correlation of the echo with a driving field, and the average echo intensity.

In slab geometry, under plane-wave illumination at normal incidence, statistical quantities are invariant by translation along the transverse direction  $x$ . To spare computation time, while taking care of finite-size effects, we combine average over  $N_{\text{conf}} = 200000$  configurations with limited range integration over  $x$ .

### A. Average field of the echo

As observed in Fig. 3, the analytical and the numerical approaches consistently describe the echo ballistic intensity variation with the depth inside the slab, although the analytical expression is derived under the diffusion approximation, valid only at large depths (i.e.  $z \gg \ell$ ).

### B. Correlation of photon echoes with the driving fields

Figure 4 gives the evolution of the correlation of the echo field with one of the driving fields as a function of

the depth inside the slab. Again a good agreement is clearly obtained between the analytical calculation and the numerical model. Nevertheless, the analytical result is not fully quantitative. Two potential effects have been identified to explain this discrepancy. First the validity of the diffusion approximation can be questioned. In the linear regime, the agreement between the diffusion equation theory and the coupled-dipole simulation is very good as shown in Fig. 2 even for small depths. However when non-linearities are present, there is potentially an accumulation of errors because of the recursion in the diffusion model provided by Eqs. (36) and (63). For small and intermediate depths, the Radiative Transfer Equation (RTE) could be a good candidate for a refined model valid at all depth [37]. However the main drawback is that analytical results do not exist for the RTE in a slab geometry. Second and potentially more important, the signal is very sensitive to the boundaries in the presence of non-linear effects. This has been checked numerically by changing the transverse size  $D$  of the pseudo-slab geometry and the results show that converged results are hard to obtain.

### C. Average intensity of the echo

Regarding the average intensity of the echo signal, the numerical results are presented in Fig. 5. Although qualitative agreement is preserved (confirming that the analytical theory captures the main physical mechanisms), a larger discrepancy is found between the theory and the simulations than for the correlation. The reasons are the same: finite transverse size effects in presence of non-linearity and validity of the diffusion approximation.

## VII. CONCLUSION

We have presented a theoretical study of photon echo generation in disordered scattering media. Developed in terms of Feynman-Dyson diagrams, the multiple scattering statistical approach has been validated by *ab initio* numerical simulations.

According to previous experiments [23], the driving fields and the echo beam stay strongly correlated as they propagate through the disordered medium. The theory has confirmed this paradoxical feature, and provided some physical insight. In the buildup of any two-field observable, such as diffuse intensity or diffuse correlation, the same dominant diagrams emerge: those that make both fields follow a common path through the disordered medium. This single propagation scheme explains the similar size of those different quantities, and the large size of the normalized correlation.

Another noticeable result is the strong enhancement of the echo by the disordered medium, in comparison with echo emission in the corresponding homogeneous material with the same concentration of active atoms. This

might open the way to applications in energy conversion.

The present work has been confined to signal investigation inside the disordered material. To be consistent with experimental conditions, we should consider signal collection outside the material, on a large aperture detector. This issue is deferred to a future work. Encouraged by the present promising results, we also plan to refine the analysis in such directions as that of the RTE, with the help of Monte Carlo simulations.

## ACKNOWLEDGMENTS

We thank Philippe Goldner for the stimulated discussions that initiated this work. We are also grateful to Thierry Chanelière for helpful comments and advices. This research is supported by the French national grant RAMACO no. ANR-12-BS08-0015-02 and by LABEX WIFI (Laboratory of Excellence within the French Program “Investments for the Future”) under references ANR-10-LABX-24 and ANR-10-IDEX-0001-02 PSL\*.

- 
- [1] L. L. Foldy, Phys. Rev. **67**, 107 (1945).  
 [2] M. Lax, Rev. Mod. Phys. **23**, 287 (1951).  
 [3] M. Lax, Phys. Rev. **85**, 621 (1952).  
 [4] M. P. Van Albada and A. Lagendijk, Phys. Rev. Lett. **55**, 2692 (1985).  
 [5] P.-E. Wolf and G. Maret, Phys. Rev. Lett. **55**, 2696 (1985).  
 [6] D. Wiersma, Nat. Phys. **4**, 359 (2008).  
 [7] V. E. Kravtsov, V. M. Agranovich, and K. I. Grigorishin, Phys. Rev. B **44**, 4931 (1991).  
 [8] M. Baudrier-Raybaut, R. Haidar, P. Kupecek, P. Lemason, and E. Rosencher, Nature **432**, 374 (2004).  
 [9] X. Wen, S. Chen, and D. D. Dlott, J. Opt. Soc. Am. B **8**, 813 (1991).  
 [10] J. F. de Boer, A. Lagendijk, R. Sprik, and S. Feng, Phys. Rev. Lett. **71**, 3947 (1993).  
 [11] C. Vanneste and P. Sebbah, Phys. Rev. Lett. **87**, 183903 (2001).  
 [12] H. Cao, J. Y. Xu, D. Z. Zhang, S. H. Chang, S. T. Ho, E. W. Seelig, X. Liu, and R. P. H. Chang, Phys. Rev. Lett. **84**, 5584 (2000).  
 [13] T. Wellens and B. Grémaud, Phys. Rev. Lett. **100**, 033902 (2008).  
 [14] T. Wellens and B. Grémaud, Phys. Rev. A **80**, 063827 (2009).  
 [15] N. A. Kurnit, I. D. Abella, and S. R. Hartmann, Phys. Rev. Lett. **13**, 567 (1964).  
 [16] I. D. Abella, N. A. Kurnit, and S. R. Hartmann, Phys. Rev. **141**, 391 (1966).  
 [17] T. W. Mossberg, Opt. Lett. **7**, 77 (1982).  
 [18] V. Markushev, N. Ter-Gabriélyan, C. Briskina, V. Belan, and V. Zolin, Quantum Electron. **20**, 773 (1990).  
 [19] M. Colice, F. Schlottau, K. Wagner, R. Mohan, W. Babbitt, I. Lorgeré, and J.-L. Le Gouët, in *Proceedings of SPIE*, Vol. 5557 (2004) p. 132.  
 [20] J.-L. Le Gouët, F. Bretenaker, and I. Lorgeré, in *Advances In Atomic, Molecular, and Optical Physics*, Vol. 54, edited by P. R. Berman, C. C. Lin, and E. Arimondo (Elsevier, 2007) pp. 549–613.  
 [21] W. Tittel, M. Afzelius, R. Cone, T. Chanelière, S. Kroll, S. Moiseev, and M. Sellars, Laser & Photon. Rev. **1**, 1863 (2009).  
 [22] H. de Riedmatten, M. Afzelius, M. U. Staudt, C. Simon, and N. Gisin, Nature **456**, 773 (2008).  
 [23] F. Beaudoux, A. Ferrier, O. Guillot-Noël, T. Chanelière, J.-L. Le Gouët, and P. Goldner, Opt. Express **19**, 15236 (2011).  
 [24] A. Perrot, P. Goldner, D. Giaume, M. Lovrić, C. Andriamiadamanana, R. R. Gonçalves, and A. Ferrier, Phys. Rev. Lett. **111**, 203601 (2013).  
 [25] T. W. Mossberg, R. Kachru, S. R. Hartmann, and A. M. Flusberg, Phys. Rev. A **20**, 1976 (1979).  
 [26] V. E. Kravtsov, V. M. Agranovich, and K. I. Grigorishin, Phys. Rev. B **44**, 4931 (1991).  
 [27] T. Ito and M. Tomita, Phys. Rev. E **69**, 036610 (2004).  
 [28] S. E. Skipetrov, J. Opt. Soc. Am. B **21**, 168 (2004).  
 [29] M. C. W. van Rossum and T. M. Nieuwenhuizen, Rev. Mod. Phys. **71**, 313 (1999).  
 [30] E. Akkermans and G. Montambaux, *Mesoscopic Physics of Electrons and Photons* (Cambridge University Press, Cambridge, 2007).  
 [31] U. Frisch, *La propagation des ondes en milieu aléatoire et les équations stochastiques* (Institut d’Astrophysique, 1967).  
 [32] F. Dyson, Phys. Rev. **75**, 486 (1949).  
 [33] F. Dyson, Phys. Rev. **75**, 1736 (1949).  
 [34] S. M. Rytov, Y. A. Kravtsov, and V. I. Tatarskii, *Principles of Statistical Radiophysics*, Vol. 4 (Springer-Verlag, Berlin, 1989).  
 [35] L. A. Apresyan and Y. A. Kravtsov, *Radiation Transfer: Statistical and Wave Aspects* (Gordon and Breach Publishers, Amsterdam, 1996).  
 [36] A. Ishimaru, *Wave Propagation and Scattering in Random Media* (IEEE Press, Oxford, 1997).  
 [37] S. Chandrasekhar, *Radiative Transfer* (Dover, New-York, 1950).